A Conserved Landscape of Chemokine Receptor Co-expression Defines the Functional States of CD8+ T Cells in Melanoma

Authors: Rodney Macedo[1,2]*, David. W. Harle[1,2], Kevin Hoffer-Hawlik[3], Ximi K. Wang[1,2], Thomas McMahon-Skates[1], Alexandra Matschiner[1], Kirubel Belay[1], Yvonne M. Saenger[4], Benjamin Izar[1,2,8], Elham Azizi[2,3,5,6,7], Ran Reshef[1,2,8]*

Affiliations:

[1]Columbia Center for Translational Immunology, Department of Medicine, Columbia University Irving Medical Center, New York, NY 10032, USA.

[2]Herbert Irving Comprehensive Cancer Center, Columbia University Irving Medical Center, New York, NY 10032, USA

[3]Department of Biomedical Engineering, Columbia University, New York, NY, USA. Irving Institute for Cancer Dynamics, Columbia University, New York, NY 10027, USA.

[4]Department of Oncology, Albert Einstein College of Medicine, Bronx, NY 10461, USA.

[5]Irving Institute for Cancer Dynamics, Columbia University, New York, NY, 10027, USA.

[6]Department of Computer Science, Columbia University, New York, NY, 10027, USA.

[7]Data Science Institute, Columbia University, New York, NY, 10027, USA.

[8]Department of Medicine, Division of Hematology & Oncology, Columbia University Irving Medical Center, New York, NY, USA.

*To whom correspondence should be addressed: ran.reshef@columbia.edu, rmacedo@igtp.cat

One Sentence Summary: Co-expression of CCR5, CXCR6, and CXCR3 provides a functional 'code' that separates T-cell-mediated anti-tumor efficacy from off-target toxicity, enabling the selection of superior cells for safer and more effective cancer immunotherapies.

Graphical Abstract

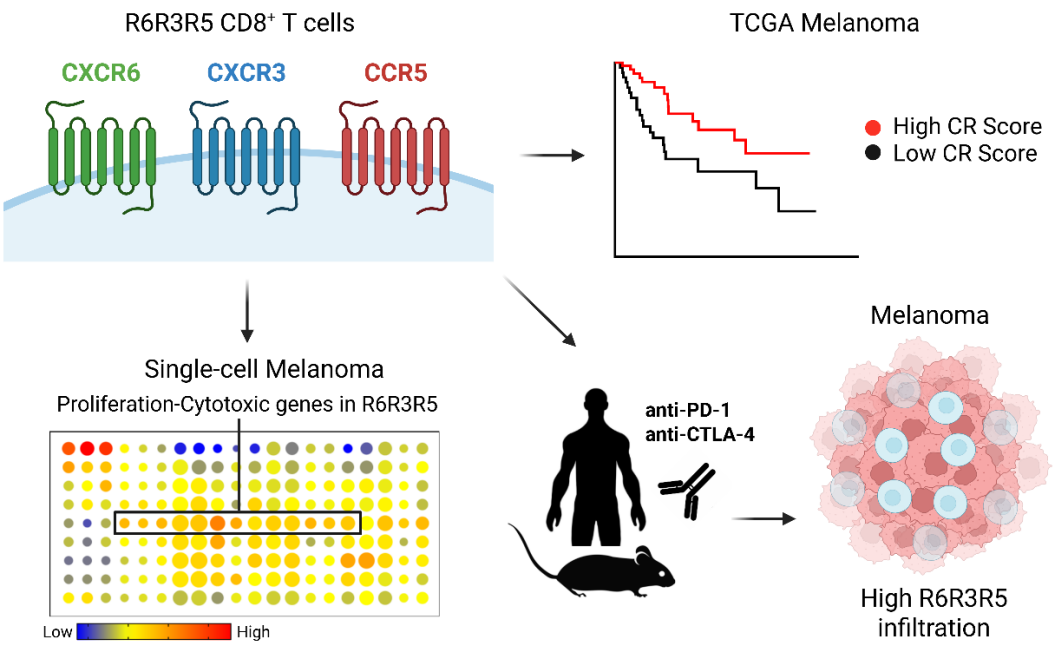

Highlights

- CXCR6, CXCR3 and CCR5 co-expression signature stratifies patient survival in human melanoma
- $CD8^+$ T cells co-expressing CXCR6, CXCR3 and CCR5 are critical effectors with high proliferative, cytotoxic, and activation profile in human and mice melanoma
- $CD8^+$ T cells co-expressing CXCR6, CXCR3 and CCR5 drive anti-tumoral responses during checkpoint blockade in both human and mice

Abstract:

Cancer immunotherapies, from checkpoint blockade to adoptive cell therapies like tumor-infiltrating lymphocytes (TILs), have revolutionized cancer treatment but are limited by variable efficacy and significant toxicities. A central challenge is identifying ideal T-cell populations that effectively eliminate tumors without causing off-target damage, a distinction not captured by existing biomarkers. We show that co-expression patterns of chemokine receptors (CRs) CXCR3, CCR5, and CXCR6 on $CD8^+$ T cells provide a functional "code" defining subsets with divergent roles in on-target immunity versus off-target inflammation. In mouse and human melanoma, a triple-positive ($CXCR3^+CCR5^+CXCR6^+$) T-cell subset is essential for tumor control, and its genetic signature correlates with positive clinical response, while a distinct $CCR5^+CXCR6^+$ subset drives liver immune-related adverse events (IRAEs). Crucially, this CR code reveals that immunotherapy actively reshapes T-cell trafficking patterns, uncovering profound heterogeneity within conventional populations and distinguishing potent anti-tumor progenitors from cells predisposed to exhaustion or off-target migration. This work establishes CR co-expression as a practical tool, providing a surface marker-based strategy to identify and enrich optimized T cells for adoptive therapies, thereby offering a framework to uncouple efficacy from toxicity.

Article:

Combined PD-1 and CTLA-4 blockade (P1C4) leads to impressive and durable clinical responses in melanoma [1], and many other cancers [2,3]. Though transformative, only a subset of patients responds, and immune-related adverse events (IRAEs) account for the high incidence of grade 3-4 adverse events, treatment-related mortality and high discontinuation rates, limiting broader application of combination therapies [4-11]. Both tumor rejection and IRAEs induced by checkpoint inhibitors are fundamentally governed by lymphocyte migration into tumors and healthy tissues [12-14]. The recent approval of autologous tumor-infiltrating lymphocytes (TILs) in metastatic melanoma and the fact that the majority of patients do not achieve long-term benefit from this approach [15-17] further underscore the need for deeper understanding of T-cell populations with an ideal profile that combines effective trafficking to the tumor, potent effector function, high proliferative capacity (stemness), ability to resist suppressive signals, and low exhaustion state, resulting in an effective anti-tumor response.

Chemokines are proteins that control the trafficking of T cells and other leukocytes into different tissues by interacting with chemokine receptors (CR) expressed on the cell surface [18]. Previous studies have investigated the role of CRs individually. Elevated expression of certain chemokine receptors such as CXCR3 and CCR5 or their ligands is associated with increased intratumoral T-cell infiltration and favorable outcomes in melanoma [19-21] and other cancers [22-27]. These studies led to the experimental use of CR inhibitors in cancer patients with mixed results [28-31], possibly due to failure to account for the biologic reality that leukocytes co-express multiple CRs which collectively orchestrate their migration and potentially other functions [32]. This highlights a significant gap in our understanding and an unmet need in identifying T-cell populations with an ideal profile - combining potent tumor trafficking and effector function while avoiding healthy tissues. This may facilitate the development of novel pharmacologic or adoptive cell therapy approaches in cancer.

Here, we address this challenge by investigating the co-expression patterns of key inflammatory CRs. We provide evidence in both mice and humans that the coordinated expression of CXCR3, CCR5, and CXCR6 defines distinct $CD8^+$ T-cell subsets with divergent roles in mediating tumor clearance and immune-related toxicity following dual checkpoint blockade. Our findings may help design future therapies that modulate leukocyte migration to improve the efficacy and reduce immune-related toxicity of cancer immunotherapies.

A T-cell Chemokine Receptor Signature Stratifies Patient Survival in Melanoma

To identify CRs central to the anti-tumor T-cell response and conserved across multiple cancers, we conducted an *in-silico* analysis of 11,323 tumor transcriptomes from 33 human cancers in the Cancer Genome Atlas (TCGA). This screen revealed that the inflammatory CR genes *CXCR3*, *CCR5*, and *CXCR6* exhibit both high expression and variance (Extended Data Fig. 1a). This receptor triad forms a distinct signature that strongly correlated with T-cell specific genes compared to other leukocyte populations (Fig. 1a top and Supplementary Table 1). This patter was conserved in 475 human melanoma samples (Fig. 1a bottom and Extended Data Fig. 1b). Consistent with this, the primary ligands for CXCR3, CCR5 and CXCR6 correlated with T-cell- and macrophage-specific genes, but not with tumor cells, B cells or fibroblasts (Extended Data Fig. 1c).

While individual receptor expression was higher in "brisk" tumors [33] (characterized by dense lymphocytic infiltrate) versus "non-brisk" PANCAN and melanoma tumors, a combinatorial CR score proved superior for stratification. Specifically, CR scores (based on *CXCR6*, *CXCR3* and *CCR5* expression) were not only associated with significant differences between these tumor types (Fig. 1b, Extended Data Fig. 1d) but also linked to improved overall survival uniquely within brisk tumors (Fig. 1c). Furthermore, CR scores correlated with higher abundance of $CD8^+$ T cells [34] and IFN-γ signatures [35] in tumors, predicting a survival benefit even within $CD8^+$ and IFN-γ-dominant tumors (Fig. 1c, Extended Data Fig. 1e-g). This was reinforced by an analysis of transcriptional data from metastatic [36] and primary [37] human melanoma confirming that higher CR scores associate with non-recurrent (Extended Data Fig. 1h) and responder (Extended Data Fig. 1i) tumors, respectively. Differentially expressed genes (DEGs) in samples with high *CXCR6*, *CXCR3*, and *CCR5* co-expression were enriched for T cell activation pathways (Extended Data Fig. 1j and 1k). Collectively, these data establish *CXCR3*, *CCR5*, and *CXCR6* as a core inflammatory T-cell signature associated with improved survival.

Combinatorial Chemokine Receptor Expression Reveals a Hierarchy of T-cell Effector Programs

To determine if CR co-expression patterns define distinct functional states, we performed *in-silico* single-cell analysis of treated and untreated human metastatic melanoma tumors [38]. Focusing on $CD8^+$ T cells ($CD8^+$), after identifying major cell populations (Extended Data Fig. 2a) using cell type-specific genes, we classified nine unique subsets based on the combinatorial expression of *CXCR6*, *CXCR3* and *CCR5* (using *CCR7* to demarcate naive cells) (Fig. 1d left). This approach revealed extensive CR heterogeneity in the tumor microenvironment (TME) (Fig. 1d right) and demonstrated that multi-receptor patterns, rather than single markers, are required to delineate functionally distinct cell states.

Transcriptional profiling of CR-defined subsets uncovered a functional continuum across $CD8^+$ T cells, from naive to terminally differentiated states (Fig. 1e-f, Extended Data Fig. 2b-c, and Supplementary Table 2). At one end of the spectrum, the triple-negative (3N+) and CXCR3-only (R3) subsets were the least differentiated, expressing markers of stemness and a naive state, alongside chemokines involved in dendritic cells recruitment, suggesting a progenitor-like role. In contrast, co-expression of CCR5 and/or CXCR6 marked cells with potent effector programs. The **triple-positive (R6R3R5) subset** emerged as a critical effector phenotype, exhibiting the highest expression of proliferation, cytotoxicity, and activation genes. Dual-expressing subsets represented distinct intermediate states; R3R5 TILs were highly proliferative, while R6R3 TILs displayed a resident-effector profile with high expression of cytotoxic molecules but lower proliferation. Finally, CXCR3-negative TILs appeared terminally differentiated, characterized by high expression of exhaustion markers. Within this group, R5 cells resembled an immature memory state, while R6R5 and R6 subsets were more akin to short-lived effector cells, with R6R5 being more cytotoxic and R6 showing more tissue residency markers. These findings indicate that specific combinations of CXCR3, CCR5, and CXCR6 define a detailed functional map of $CD8^+$ T cell diversity within the TME.

Chemokine Receptor Expression Marks a Differentiation and Activation Trajectory in TILs

To map the evolution of CR expression during T cell maturation, we analyzed a second human metastatic melanoma single-cell RNA-seq dataset [39]. We applied pseudotime inference (Extended Data Fig. 2d-e), a computational approach which orders cells along a continuous phenotypic trajectory, in this case from naive (*TCF7*-expressing) to terminally differentiated (*TOX*-expressing) $CD8^+$ T cells [40]. Sliding window analysis of gene expression revealed a distinct, sequential pattern of CR expression along this differentiation trajectory (Fig. 1g). The trajectory begins with high *CCR7* expression, which is progressively lost (Fig. 1h). *CXCR3* emerges early and is sustained, whereas *CCR5* appears and peaks in intermediate states. Finally, *CXCR6* expression is acquired late, marking the most differentiated cells and correlating with *TOX* expression. Taken together, these results suggest that T-cell maturation within the tumor involves programmed, sequential co-expression of *CXCR3*, *CCR5* and *CXCR6* followed by a gradual loss of these receptors in the terminally differentiated phase. This evolution underscores that dynamic combinatorial patterns, rather than static expression of a single receptor, are critical for accurately characterizing the functional state of TIL subsets and their distinct roles in mediating anti-tumor efficacy.

A Conserved Chemokine Receptor Code Defines Functional T-cell Programs in Mice and Humans

We next validated these CR-defined subsets at the protein level using multiparametric flow cytometry in healthy human and mouse lymphocytes (Fig. 2a, Extended Data Fig. 3 and Supplementary Table 3). This analysis revealed that the CR co-expression "code" is a conserved feature that defines a functional hierarchy (Fig. 2b-c, Extended Data Fig. 4a-c). In both species, the least differentiated, naive-like subsets (3N+ and R3) were the most abundant and largely corresponded to traditional Naive (T_N) and Central Memory (T_{CM}) populations. In contrast, the Effector Memory (T_{EM}) population was highly heterogeneous, comprising the full spectrum of CR-defined subsets (Fig. 2d-e, Extended Data Fig. 4d-f).

Crucially, our CR framework uncovered profound functional divergence within the classically defined TEM population (Fig. 2f and Extended Data Fig. 4g). For example, R3 T_{EM} cells retained stem-like properties (high TCF1/7), while subsets co-expressing multiple CRs, such as R6R3R5, were primed for cytotoxicity and proliferation. Other subsets showed exhausted phenotypes (high PD-1, LAG3) or distinct tissue-homing potentials, expressing receptors that support either tumor infiltration (CCR2) or mucosal sites (CCR6, CCR9). These results confirm at the protein level that CR co-expression defines conserved, functionally distinct T-cell subsets and resolves critical heterogeneity within the traditional T_{EM} population, distinguishing cells with potent anti-tumor potential (R6R3R5) from those predisposed to exhaustion or migration to other tissues.

Distinct T-cell CR Subsets Drive On-Target Efficacy Versus Off-Target Inflammation During Checkpoint Blockade

To dissect the *in vivo* roles of CR-defined subsets in the context of immunotherapy, we studied their response to dual PD-1 and CTLA-4 blockade (P1C4) in a B16-F10 melanoma model (Fig. 3a). This combination was chosen as it was most effective at increasing $CD8^+$ T_{EM} cells compared to single-agent therapy (Extended Data Fig. 5a) and is clinically relevant due to its high efficacy in human melanoma. Treatment increased $CD8^+$ T and T_{EM} percentages in both tumor and liver (Fig. 3b). While liver enzymes remained unchanged in this model, immunohistochemistry revealed a

172 significant increase in $CD3^+$ T cells in the liver, indicating subclinical inflammation (Extended Data
173 Fig. 5c-e). These results established a robust model to simultaneously investigate tumor control
174 and tissue-specific drivers of early immune-related toxicity.

175 P1C4 therapy profoundly and selectively altered the distribution of CR-defined subsets in
176 peripheral tissues (Fig. 3c). In the tumor, treatment drove a dramatic expansion of the triple-
177 positive R6R3R5 subset. Conversely, in the liver, P1C4 selectively increased the R6R5 subset.
178 These tissue-specific effects were not observed in the spleen or tumor-draining lymph nodes
179 (TdLNs)(Extended Data Fig. 5f). This divergence suggests that distinct CR programs mediate on-
180 target anti-tumor activity versus off-target immune infiltration. This conclusion is also supported
181 by a corresponding increase in the ligands for CXCR3, CCR5 (e.g., CXCL9, CXCL10, CCL5) in both
182 tumor and liver supernatants after treatment, whereas CXCR6 ligand (CXCL16) is higher only in
183 the tumor (Extended Data Fig. 5g).

184 Using genetic knockout models, we demonstrated that CR co-expression is essential for
185 therapeutic efficacy. In *CCR5*- or *CXCR6*-deficient mice, P1C4 failed to increase intratumoral $CD8^+$
186 T_{EM} cells, losing any significant change in CR-defined subsets (Fig. 3d-e). Furthermore, the P1C4-
187 mediated improvement in the $CD8^+$/Treg ratio was blunted in *CCR5*-knockout mice and
188 eliminated in *CXCR6*-knockout mice (Fig. 3f). These data demonstrate that an optimal anti-tumor
189 response to P1C4 requires the functional contribution of T cells able to express all three
190 receptors.

191 A competitive short-term homing assay further clarified CR roles (Fig. 3g). As expected, CXCR3 is
192 critical for T-cell trafficking into the tumor, TdLNs, and liver following P1C4 treatment (Fig. 3h and
193 Extended Data Fig. 5h-i). The roles of the other receptors are more complex; for instance, *CXCR6*-
194 deficient cells accumulate in lymphoid tissues after P1C4 treatment, suggesting impaired
195 migration to the tumor or inability to establish tissue residency status. Altogether, these data
196 establish that the functional outcome of P1C4 therapy—tumor rejection versus immune-
197 mediated toxicity—relies on the specific co-expression of CXCR3, CCR5, and CXCR6 on responding
198 T cells.

199 **Anti-Tumor T-cell Subsets Defined by CR Co-expression Expand with Checkpoint Blockade and**
200 **Correlate with Clinical Response**

201 To validate our findings clinically, we analyzed PBMCs from melanoma patients, comparing
202 Immune Checkpoint Blockade (ICB)-treated and ICB-naive patients (Supplementary Table 4). ICB-
203 treated patients had significantly higher percentages of $CD8^+$ T cells in their blood compared to
204 ICB-naive patients (Extended Data Fig. 6a-b). Strikingly, dual ICB treatment led to a significant
205 expansion of the circulating triple positive R6R3R5 subset (Fig 4a), mirroring our findings in
206 murine splenic $CD8^+$ T cells (Extended Data Fig. 6c).

207 ICB remodeled the overall profile and immunophenotype of CR-defined subsets (Fig. 4b-c).
208 Interestingly, ICB treatment was associated with significantly decreased AhR in 3N+ and R3
209 subsets, while R6 subsets exhibited increased KLRG1. Several subsets (R5, R3R5, R6R3R5, R6R5)
210 showed declined PD-1 expression, suggesting receptor occupancy by therapeutic antibody [41].
211 These results confirm in humans that P1C4 treatment increases the proportion of CR-defined

212 subsets responsible for tumor control but also modifies the functional properties of these
213 subsets.

214 Finally, to determine if CR-defined subsets within the human TME are associated with clinical
215 outcomes, we analyzed the single-cell transcriptional dataset from metastatic melanoma
216 patients treated with ICB [39]. This analysis revealed that *CXCR6* expression was significantly higher
217 (P=0.0095) in responder than non-responders (Extended Data Fig. 6d). Importantly, gene
218 signatures for CXCR6-co-expressing subsets - R6R3R5, R6R3 and R6R5- were significantly
219 enriched in tumors of responder patients (P<0.05) (Fig. 4d). These results confirm that ICB
220 reshapes the circulating T cell landscape to favor the highly functional R6R3R5 subset. Critically,
221 they also establish that the enrichment of CXCR6-co-expressing T-cell subsets within the tumor
222 itself is a key feature of a successful anti-tumor response to immunotherapy.

223 **Discussion**

224 A central challenge in cancer immunotherapy—from checkpoint blockade to adoptive cell
225 therapies like TILs—is uncoupling potent anti-tumor efficacy from treatment-limiting, off-target
226 toxicity. This requires a deeper understanding of the T-cell subsets that mediate these opposing
227 outcomes. While the roles of individual chemokine receptors in T-cell trafficking are well-studied,
228 the combinatorial "code" they form to dictate specific functional states has remained unclear.
229 Our study addresses this gap, demonstrating that the co-expression of CXCR3, CCR5, and CXCR6
230 provides a conserved functional map of $CD8^+$ T cells in both mice and humans, allowing for the
231 prospective identification of T-cell subsets responsible for on-target efficacy versus off-target
232 inflammation.

233 Our analysis reveals that this CR code defines a fundamental and conserved T-cell developmental
234 trajectory. In healthy individuals, we found that the hierarchy progresses from naive-like,
235 progenitor cells expressing primarily CXCR3 (R3 subset) to highly differentiated effector cells co-
236 expressing all three receptors (R6R3R5 subset). Crucially, this framework uncovers profound
237 functional heterogeneity within traditionally defined populations like effector memory T cells
238 (T_{EM}). Within the T_{EM} pool, our code distinguishes stem-like progenitors (R3) from highly cytotoxic
239 and proliferative effectors (R6R3R5) and exhausted subsets, a level of functional resolution not
240 achievable with conventional markers. Importantly, our analysis demonstrates that specific
241 combinations of these three receptors, rather than single markers, are required to accurately
242 define the functional state and potential of a T cell.

243 In the context of cancer immunotherapy, this framework provides a powerful lens to dissect the
244 mechanisms of both tumor response and IRAEs. Our preclinical data show that dual ICB
245 selectively expands the triple-positive R6R3R5 subset in the tumor, a population essential for
246 therapeutic efficacy. Conversely, the therapy promoted the accumulation of a distinct
247 $CCR5^+CXCR6^+$ (R6R5) subset in the liver, a common site of IRAEs. This finding mechanistically links
248 a specific, identifiable T-cell subset to off-target toxicity, providing a cellular target for future
249 strategies aimed at mitigating IRAEs. The fact that genetic deletion of either CCR5 or CXCR6
250 abrogated the therapeutic effect of ICB underscores that the coordinated function of all three

251 receptors on the R6R3R5 subset is non-redundant and essential for a successful anti-tumor
252 response.

253 Ultimately, our findings set up this CR code not just as a prognostic biomarker but as a practical
254 tool for developing better immunotherapies. The prognostic value of single chemokine receptors
255 has been inconsistent across studies, likely because, as we show, the functional output of T cells
256 is associated with receptor combinations. The true translational potential of our work lies in its
257 direct application to cell-based therapies. The surface markers of this code are readily detectable
258 by high-dimensional flow cytometry, offering a straightforward strategy to identify and
259 prospectively isolate the most desirable T-cell populations. For adoptive cell therapies, such as
260 TILs, this framework provides a clear rationale for enriching the final product with the highly
261 proliferative and cytotoxic R6R3R5 subset while potentially depleting populations like R6R5 that
262 may contribute to toxicity. This approach offers a tangible path forward to engineer more potent
263 and safer immunotherapies, improving the therapeutic window by maximizing anti-tumor
264 activity while minimizing collateral damage.

265 While the expression profile of CRs and other trafficking molecules in immune cells has been
266 previously described in healthy humans [42,43] and in cancer [44,45], the functional impact of their co-
267 expression on the anti-tumor response requires multiparametric, single-cell analysis. Using
268 genetic datasets and high-dimensional flow cytometry, our study simultaneously analyzed
269 multiple CRs with functional markers and transcription factors to clarify the critical role of CR co-
270 expression in shaping anti-tumor T-cell responses.

271 **Data and code availability**

272 All data generated in this study are included in this published article and its supplementary
273 information. Code relating to data processing and figure generation is available in our GitHub
274 repository. Patient information is available on the supplementary table 4. Any additional
275 information required to reanalyze the data reported in this paper is available from the
276 corresponding authors upon request.

277 **Acknowledgements**

278 We thank the CCTI Biobank and Flow Cytometry Cores. We gratefully acknowledge the Columbia
279 Institutional Review Board and all patients who generously consented to participate in this study,
280 as well as the Institutional Animal Care and Use Committee. We are also grateful to Megan Sykes,
281 Siu-Hong Ho, Audrey Baeyens, and Claudia Gutierrez-Chavez for helpful discussions.

282 **Funding**

283 E.A. is supported by NIH NCI R00CA230195, NHGRI R01HG012875, and grant number 2022-
284 253560 from the Chan Zuckerberg Initiative DAF, an advised fund of Silicon Valley Community
285 Foundation. E.A. and R.R. are supported by a Columbia University HICCC programmatic pilot
286 award. R.R. is supported by NIH R01-HL143424, P30-CA013696, and CA171008(DOD) grants.
287 J.L.M. is supported by NIH NHGRI R35HG011941 and NSF CBET 2146007. The CCTI/HICCC Flow
288 Cytometry Core is supported by NIH grants S10OD020056 and S10OD030282.

289 **Author contributions**

R.M., D.H., and R.R., conceived the study. R.M., D.H., K.H.H., X.W., A.M., and K.B. performed sample processing and data collection. R.M., D.H., K.H.H., X.W., T.M.S., K.B., Y.S., B.I., E.A., and R.R. provided clinical samples and data and maintained regulatory oversight. R.M., D.H., K.H.H., X.W., and T.M.S., analyzed the data. R.M., D.H., K.H.H., X.W., T.M.S., A.M., K.B., Y.S., B.I., E.A., and R.R. interpreted the data. R.M., R.R., E.A. and K.H.H. wrote the manuscript.

Declaration of interests

R.R. reports consulting or advisory role with Allogene, Bayer, Gilead Sciences, Incyte, TScan, Orca Bio, Pierre Fabre Pharmaceuticals, CareDx, Sana Biotechnology, Sail Biomedicines and Autolus, and research funding from Atara Biotherapeutics, Incyte, Sanofi, Immatics, Abbvie, Takeda, Gilead Sciences, CareDx, TScan, Cabaletta, Synthekine, BMS, J&J, Allogene, Genentech, Vittoria Therapeutics, AstraZeneca, Kinomica and Imugene.

Figure 1.

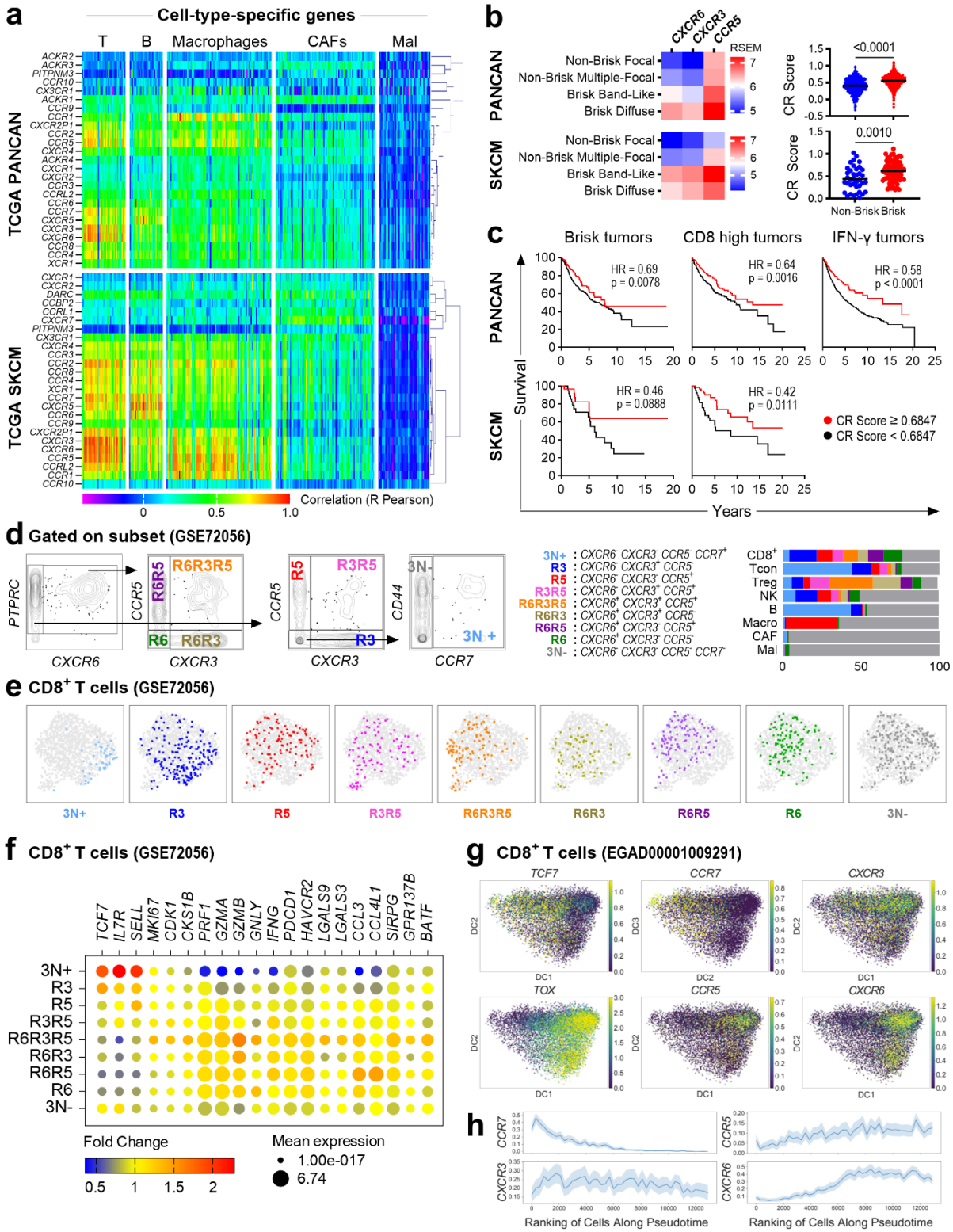
a
Cell-type-specific genes
T
B
Macrophages
CAFs
Mal
TCGA PANCAN
TCGA SKCM
Correlation (R Pearson)
b
CXCR6
CXCR3
CCR5
RSEM
PANCAN
SKCM
Non-Brisk Focal
Non-Brisk Multiple-Focal
Brisk Band-Like
Brisk Diffuse
CR Score
<0.0001
0.0010
Non-Brisk
Brisk
c
Brisk tumors
CD8 high tumors
IFN-γ tumors
HR = 0.69
p = 0.0078
HR = 0.64
p = 0.0016
HR = 0.58
p < 0.0001
HR = 0.46
p = 0.0888
HR = 0.42
p = 0.0111
Survival
Years
CR Score ≥ 0.6847
CR Score < 0.6847
d
Gated on subset (GSE72056)
PTPRC
CXCR6
CCR5
CXCR3
CD44
CCR7
R6R5
R6R3R5
R6
R6R3
R5
R3R5
R3
3N-
3N+
3N+ : CXCR6- CXCR3- CCR5- CCR7+
R3 : CXCR6- CXCR3+ CCR5-
R5 : CXCR6- CXCR3- CCR5+
R3R5 : CXCR6- CXCR3+ CCR5+
R6R3R5 : CXCR6+ CXCR3+ CCR5+
R6R3 : CXCR6+ CXCR3+ CCR5-
R6R5 : CXCR6+ CXCR3- CCR5+
R6 : CXCR6+ CXCR3- CCR5-
3N- : CXCR6- CXCR3- CCR5- CCR7-
CD8+
Tcon
Treg
NK
B
Macro
CAF
Mal
e
CD8+ T cells (GSE72056)
3N+
R3
R5
R3R5
R6R3R5
R6R3
R6R5
R6
3N-
f
CD8+ T cells (GSE72056)
TCF7
IL7R
SELL
MKI67
CDK1
CKS1B
PRF1
GZMA
GZMB
GNLY
IFNG
PDCD1
HAVCR2
LGALS9
LGALS3
CCL3
CCL4L1
SIRPG
GPR137B
BATF
Fold Change
Mean expression
1.00e-017
6.74
g
CD8+ T cells (EGAD00001009291)
TCF7
CCR7
CXCR3
TOX
CCR5
CXCR6
DC1
DC2
DC3
h
CCR7
CCR5
CXCR3
CXCR6
Ranking of Cells Along Pseudotime

Figure 1. The landscape of chemokine receptor (CR) gene expression in human cancer defines functional T-cell subsets with prognostic importance. a,b. *In-silico* analysis of tumor transcriptomes from the TCGA Pan-Cancer Atlas (PANCAN; n=11323) and melanoma (SKCM; n=475) datasets. **a.** Hierarchical clustering heatmap showing the correlation of CR gene expression with cell-type-specific genes (Supplementary Table 1) in the tumor microenvironment. **b.** Heatmaps of *CXCR6*, *CXCR3* and *CCR5* expression (left) and CR scores (right) in PANCAN and melanoma samples, stratified by "brisk" lymphocytic infiltration status. **c.** Kaplan-Meier survival curves stratified by CR score in brisk, CD8-high or IFN-γ dominant tumors. **d-f**. Single-cell transcriptomic analysis of metastatic melanoma (GSE72056). **d.** Gating strategy defining $CD8^+$ T-cell subsets based on *CXCR6*, *CXCR3*, *CCR5*, and *CCR7* co-expression (left) and heterogeneity of CR subsets across immune populations (right). **e**. UMAP projection showing CR-defined CD8+ T-cell subsets. **f**. Dot plot of gene expression for markers of naive, cytotoxicity, exhaustion, transcription factors and cytokines across CR-defined subsets. **g, h**. Diffusion mapping and pseudotime inference analysis from metastatic melanoma (EGAD00001009291) showing differential enrichment (**g**) and pseudotemporal expression patterns (**h**) of *CCR7*, *CXCR3*, *CCR5* and *CXCR6* along the *TCF7*-to-*TOX* differentiation trajectory.

Extended Data Fig. 1.

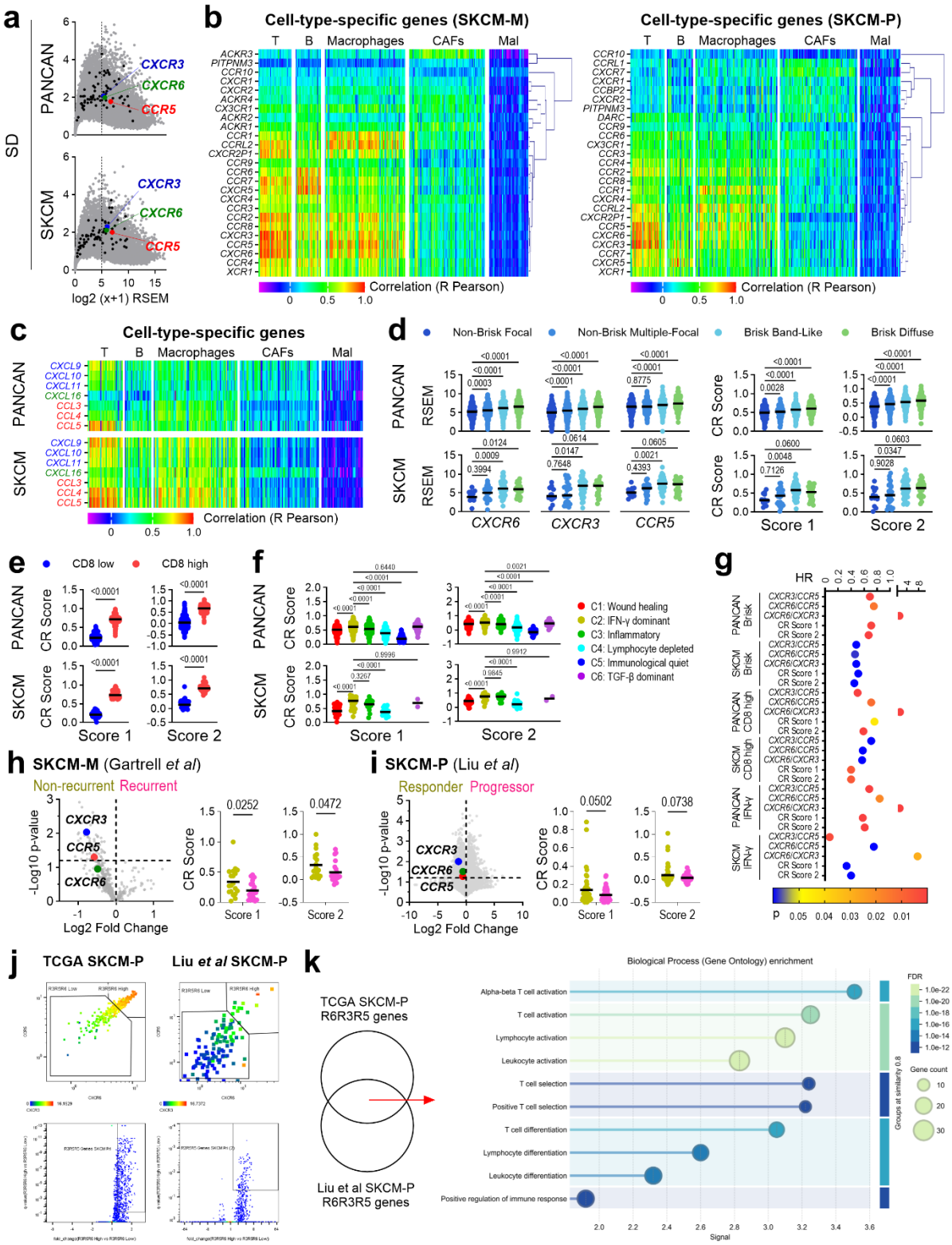

322 **Extended Data Fig. 1. Gene expression of chemokine receptors and their ligands in human**
323 **cancer.** *In-silico* analysis of tumor transcriptome from TCGA Pan-Cancer Atlas (PANCAN;
324 n=11323) and melanoma (SKCM; n=475) datasets. **a.** Mean-Variance Plot of gene expression,
325 highlighting *CXCR3*, *CCR5* and *CXCR6*. Black dots represent genes for other CRs and chemokines.
326 **b.** Hierarchical clustering heatmap of CR gene expression correlated with cell-type-specific gene
327 signatures in metastatic (SKCM-M) and primary (SKCM-P) melanoma. **c**. Hierarchical clustering
328 heatmap showing correlation of CXCR3, CCR5 and CXCR6 ligands gene expression with cell types
329 in the tumor microenvironment. **d.** Expression of individual *CXCR6*, *CXCR3, CCR5,* and
330 combinatorial CR scores (based on CXCR6, CXCR3 and CCR5 expression) across "brisk"
331 classifications. **e, f**. CR scores stratified by "$CD8^+$ score" (**e**) or immune subtype (**f**). **g**. Hazard ratios
332 (HR) for survival prediction by CR scores and CR ratios specified tumor subtypes. **h, i**. CR scores
333 in non-recurrent vs recurrent metastatic tumors (**h**) and responders vs progressors primary
334 tumors (**i**). **j**. Upregulated differentially expressed genes (DEGs) in samples with high *CXCR6*,
335 *CXCR3*, and *CCR5* co-expression. **k**. Gene Ontology analysis of shared upregulated DEGs.

336

Extended Data Fig. 2.

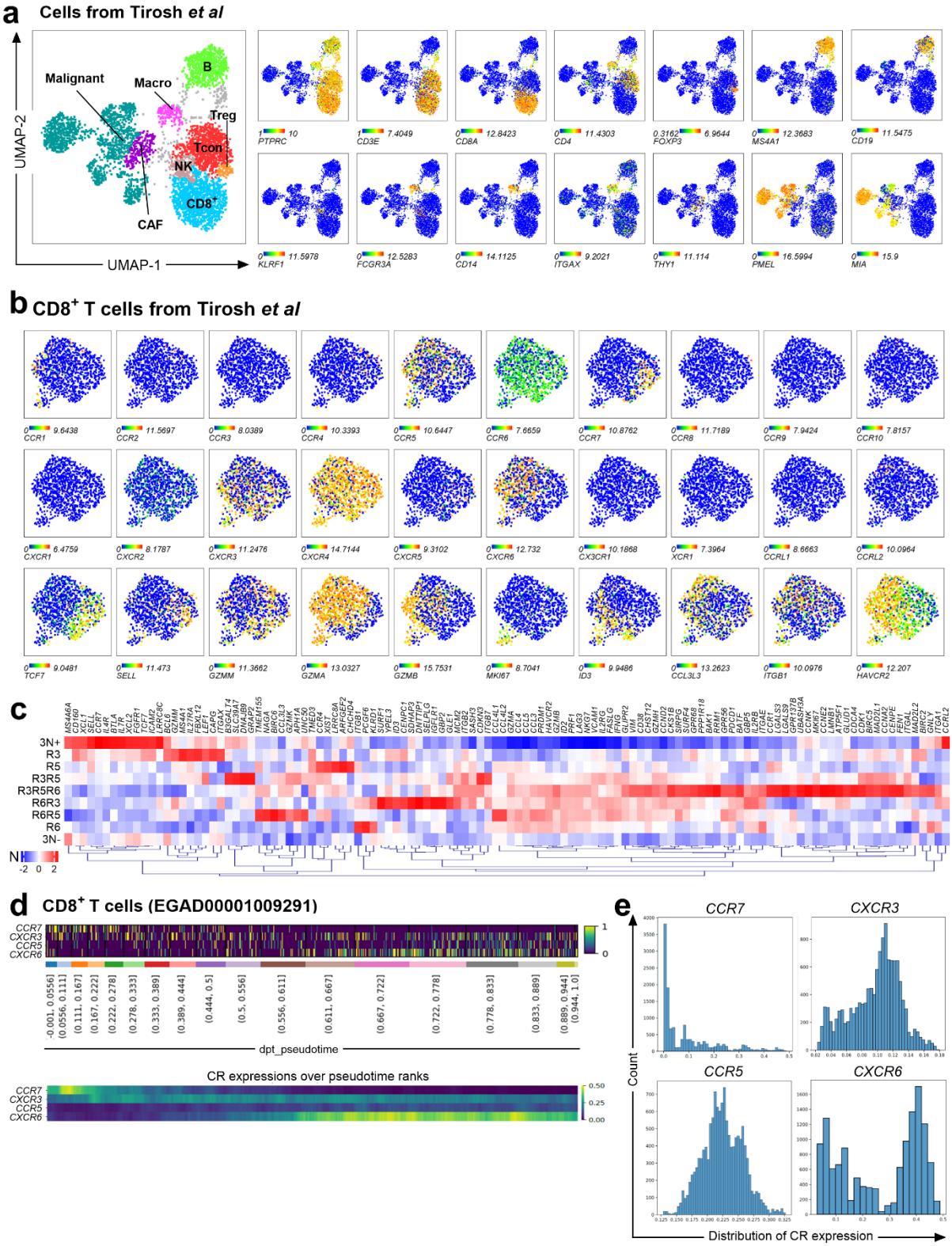

339 **Extended Data Fig. 2. a, c. Single-cell Gene expression of chemokine receptors in human**
340 **metastatic melanoma**. **a.** UMAP projection of immune populations in the tumor
341 microenvironment (GSE72056). **b.** Feature plots showing expression of naive, cytotoxicity, and
342 exhaustion markers, transcription factors and CRs in $CD8^+$ T cells. **c**. Hierarchical clustering
343 heatmap of functional markers across CR-defined CD8+ T-cells. **d, e.** Trajectory analysis of CR
344 expression in melanoma (EGAD00001009291). **d**. Rank sort and sliding window analysis (window
345 size = 300 cells) of *CCR7*, *CXCR3*, *CCR5* and *CXCR6* across pseudotime. **e.** Distributions of
346 normalized CR expression among $CD8^+$ T cells.
347

348 **Figure 2.**

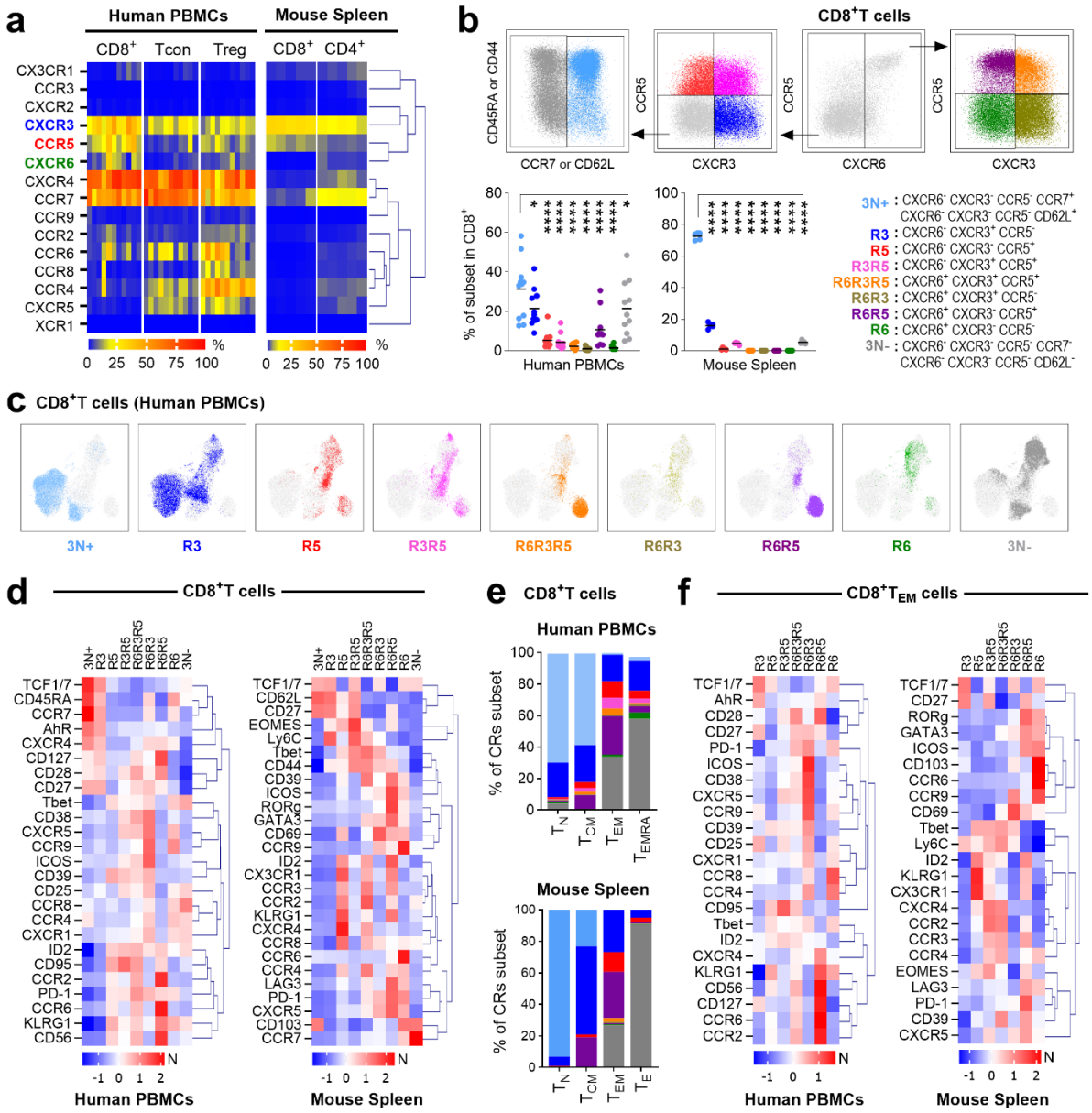

349

350 **Figure 2. Co-expression of CXCR3, CCR5 and CXCR6 defines conserved functional T-cell subsets**
351 **in humans and mice. a.** Heatmap of CR co-expression in T-cell subsets from human PBMCs (n=11)
352 and mouse splenocytes (n=5). **b.** Flow cytometry gating strategy identifying CR subsets. Scatter
353 plots show the percentages of subsets in human (left) and mouse (right) CD8$^+$ T-cells. **c**. UMAP
354 projection of CR-defined subsets in human CD8$^+$ T cells. **d**. Heatmap of normalized (N) protein
355 expression of CRs, transcription factors, activation and exhaustion markers in human and mouse
356 CD8$^+$ T cells. **e**. Distribution of CR-defined subsets within Naive (T_N), Central Memory (T_{CM}),
357 Effector Memory (T_{EM}) and effector (T_E or T_{EMRA}) populations in human and mice. **f**. Hierarchical
358 clustering heatmap of normalized (N) protein expression of CRs, transcription factors, activation
359 and exhaustion markers specifically in human and murine CD8$^+$ T_{EM} populations. Statistical

360 significance determined by unpaired Mann-Whitney tests, *P < 0.05, **P < 0.01, ***P < 0.001,
361 ****P < 0.0001.

Extended Data Fig. 3.

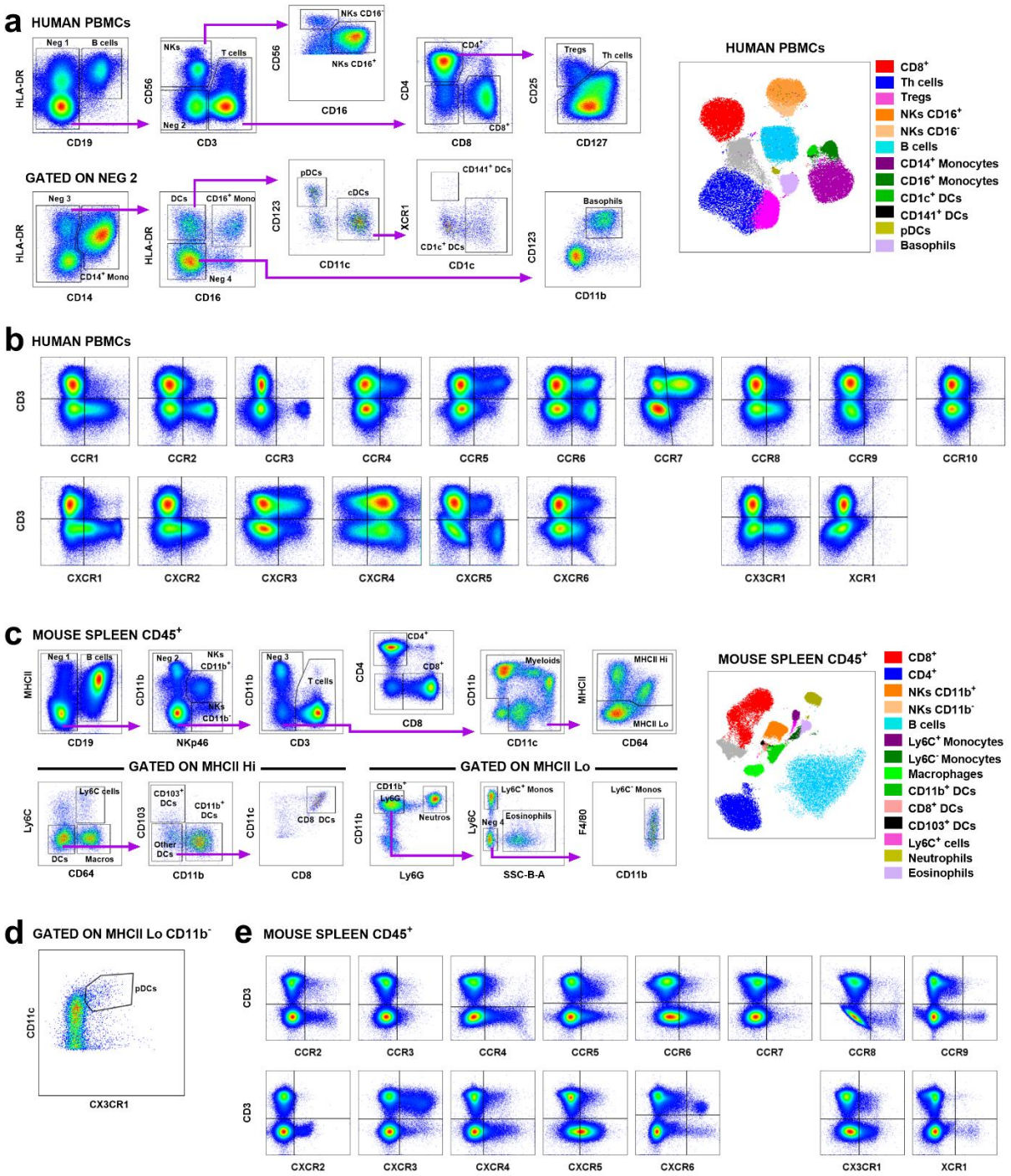

Extended Data Fig. 3. Gating strategy for spectral flow cytometry. Human PBMCs (n=11) and murine splenocytes (n=5) analyzed using a 43-color extracellular panel and 42-color intracellular panel (human) and a 36-color extracellular panel and a 35-color intracellular panel (mouse). **a.** Gating strategy and UMAP visualization for human immune subsets. **b.** Representative plots of

368 CR expression in human PBMCs. **c, d.** Gating strategy for murine immune subsets. **e.**
369 Representative plots of CR expression in murine splenocytes.
370

371 **Extended Data Fig. 4.**

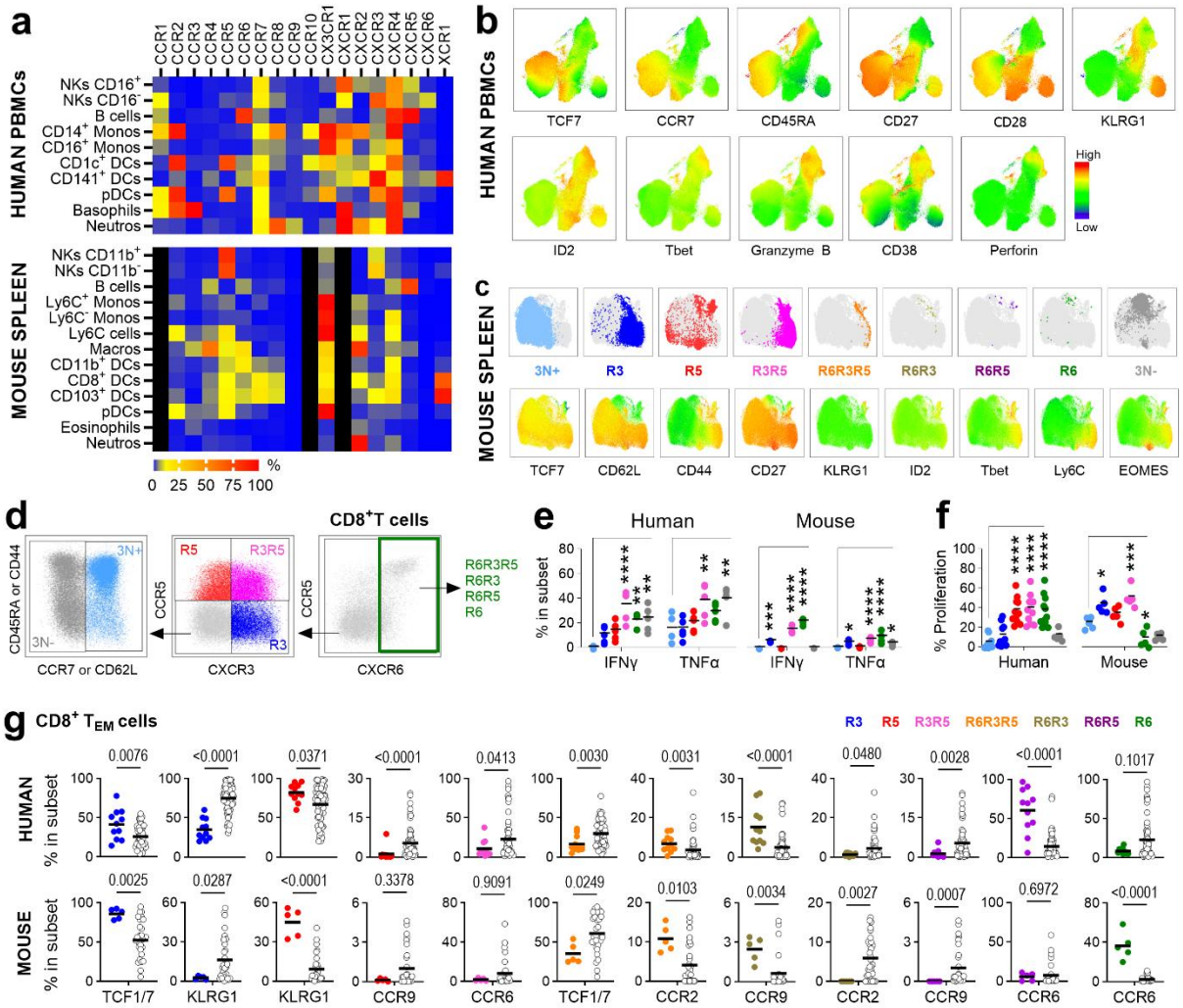

372

373 **Extended Data Fig. 4. Functional and differentiation profiles of CR-defined subsets. a**. Heatmap
374 of CR heterogeneity across immune subsets in humans and mice. Grey indicates no data. **b**. UMAP
375 projection showing functional markers in human CD8$^+$ T cells. **c**. UMAP projection of CR-defined
376 subsets overlaid with functional markers. **d-f**. Functional characterization of sorted and
377 stimulated CR-defined subsets. **d**. Gating strategy for sorting. **e, f**. Activation (**e**) and proliferation
378 (**f**) profiles of sorted subsets. **g**. Differential protein expression between specific CR subsets and
379 all other subsets (white dots). Statistical significance calculated using unpaired ANOVA or Mann-
380 Whitney multiple comparisons tests, *P < 0.05, **P < 0.01, ***P < 0.001, ****P < 0.0001.

Figure 3.

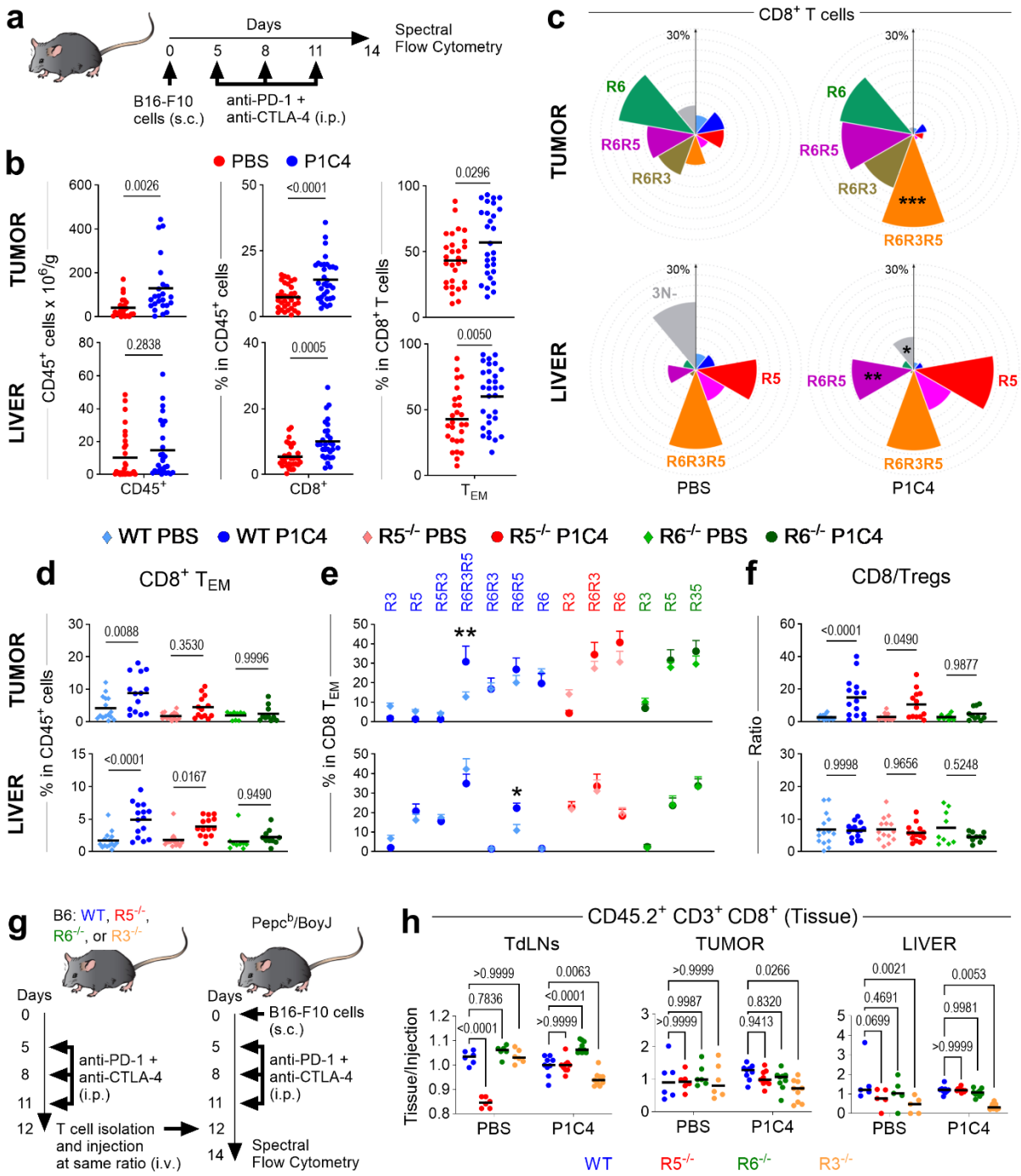

Figure 3. Triple expression of CXCR3, CCR5 and CXCR6 is required for PD-1/CTLA4-induced effector T-cell increase in melanoma. **a**. Experimental schematic: B16-F10 tumor-bearing C57BL/6J mice (n=15) were treated with PD-1/CTLA-4 (P1C4) or PBS. Cells from tumors and liver were isolated on day 14 and analyzed by spectral flow cytometry. **b.** Quantification of tumor-infiltrating CD45$^+$, CD8$^+$, and CD8$^+$ T_{EM} cells in tumor and liver. **c**. Nightingale Rose charts showing the frequency of CR-defined subsets in tumor and liver after P1C4 treatment (* to ***

389 representing significant differences between P1C4 and PBS). **d-f**. Impact of *Ccr5* (R5) or *Cxcr6* (R6)
390 deficiency on tumor (top) and liver (bottom). **d**. $CD8^+$ T_{EM} infiltration in WT, *Ccr5*$^{-/-}$ or *Cxcr6*$^{-/-}$ mice.
391 **e**. Frequency of R6R3R5 and R6R5 subsets. **f.** $CD8^+$/Treg ratio. **g.** Competitive homing assay
392 schematic. **h**. Homing ratios of $CD45.2^+$ $CD3^+$ cells in TdLNs, tumor and liver. Statistical
393 significance determined by unpaired ANOVA or Mann-Whitney multiple comparisons tests, *P <
394 0.05, **P < 0.01, ***P < 0.001, ****P < 0.0001.

Extended Data Fig. 5.

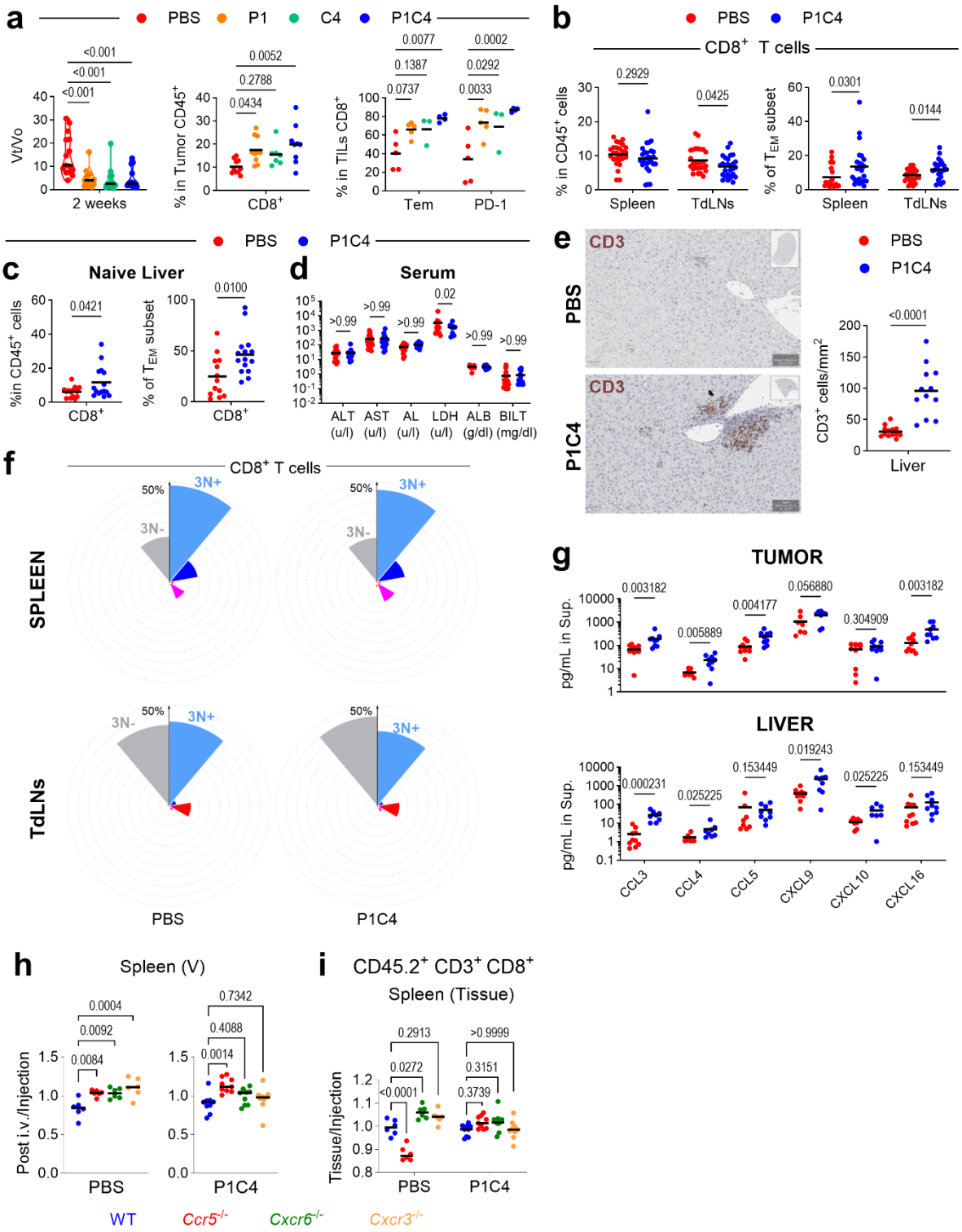

397 **Extended Data Fig. 5. Dual PD-1/CTLA4 blockade increases T_{EM} cells in tumors and target tissues**
398 **of Immune-Related Adverse Events. a, b.** Analysis of B16-F10 tumor-bearing mice (n=5-15) were
399 treated with monotherapy or combination (P1C4). **a**. Tumor volume (left, Vt = tumor volume at
400 time t and Vo = volume at baseline) and $CD8^+$ and T_{EM} (center/right). **b**. Treatment effect on
401 percentages of $CD8^+$ T cells and T_{EM} in spleen and TdLNs. **c**. Livers $CD8^+$ T_{EM} infiltration in non-
402 tumor bearing mice after treatment. **d**. Serum liver toxicity markers after treatment. **e**.
403 Immunochemistry of $CD3^+$ T-cells after treatment. **f**. Nightingale Rose of CR-defined subsets in
404 spleen and TdLNs. **g**. Concentrations of CR ligands in tumor and liver supernatants. **h, i**.
405 Competitive homing assay (described in Fig. 3i) controls showing pre-injection $CD8^+$ T proportions
406 (**h**) with a vascular increase ($CD90.2^+$) of KO cells after 48 hours and splenic tissue/injection ratios
407 (**i**). Statistical significance was calculated using unpaired ANOVA or Mann-Whitney multiple
408 comparisons tests.
409

410 **Figure 4.**

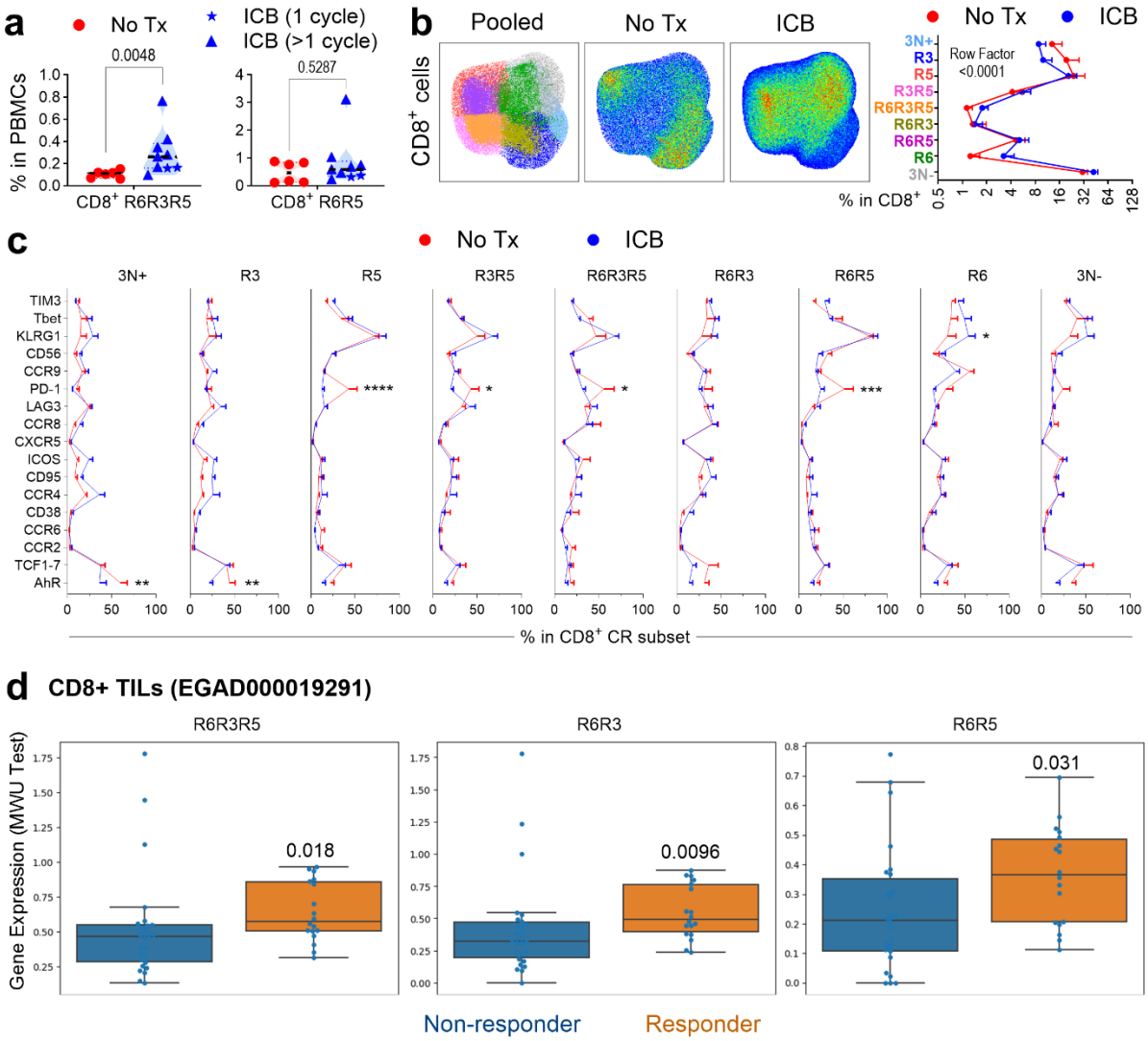

411

412 **Figure 4. PD-1/CTLA4 blockade reshapes CR co-expression in peripheral T cells of melanoma**
413 **patients. a**. Frequency of circulating CD8⁺ R6R3R5 and R6R5 in ICB-treated patients (n = 9) versus
414 untreated patients (No Tx, n = 6). **b**. UMAP projection (left) and profile plots (right) showing shifts
415 in CR subset distribution of CD8⁺ T cells following ICB. **c**. Profile plots showing phenotypic changes
416 in CRs, transcription factors, and functional markers within CD8⁺ CR-defined subsets after ICB. **d**.
417 Expression of R6R3R5, R6R3, and R6R5 gene signatures in ICB responders versus non-responders
418 (EGAD000019291). Statistical significance determined by unpaired ANOVA or Mann-Whitney
419 multiple comparisons tests, *P < 0.05, **P < 0.01, ***P < 0.001, ****P < 0.0001.

420

421 **Extended Data Fig. 6.**

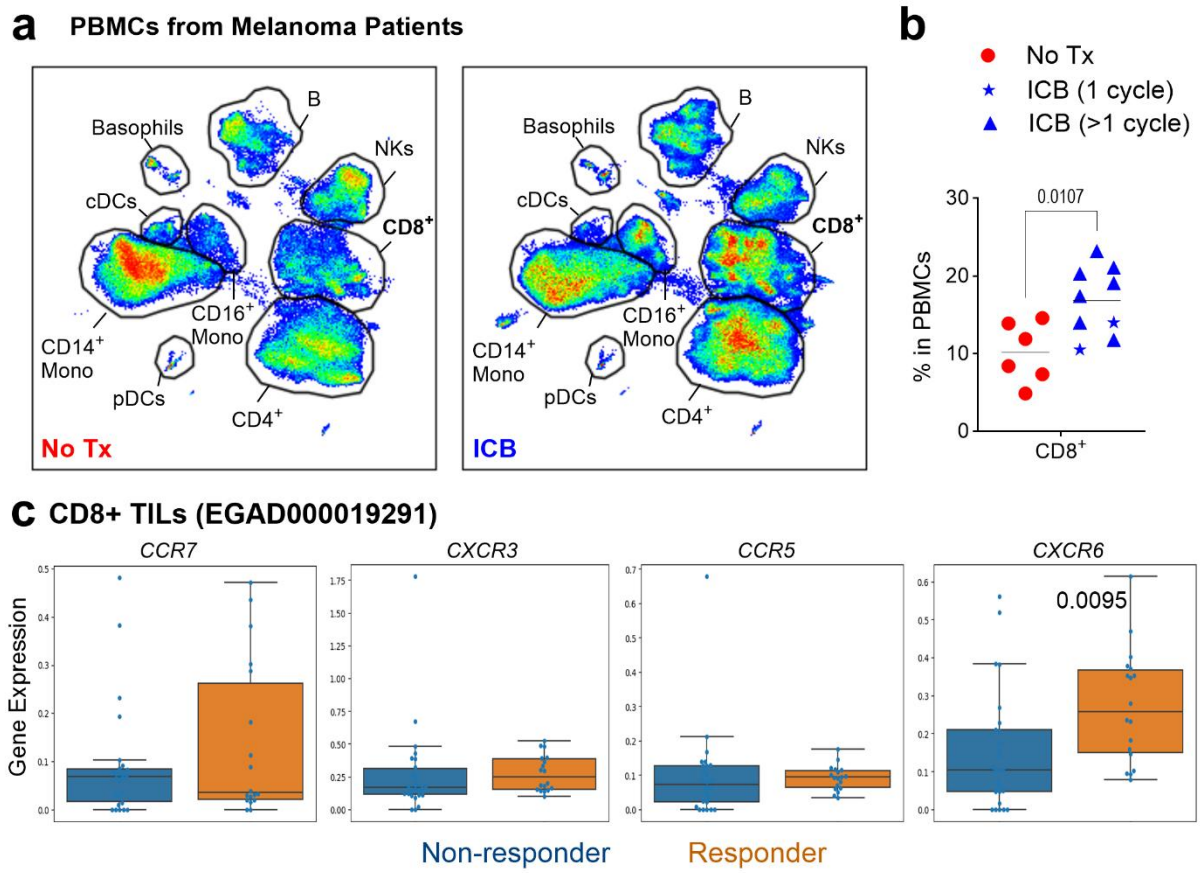

422

423 **Extended Data Fig. 6. Peripheral T cell dynamics during ICB in melanoma patients. a, b.** UMAP
424 projection (**a**) and quantification (**b**) of CD8 T^{+} cells in PBMCs of melanoma patients. **c**. CR gene
425 expression in ICB responders versus non-responders (EGAD000019291). Statistical significance
426 determined by unpaired ANOVA or Mann-Whitney multiple comparisons tests.

427 **References**

428

429 1 Wolchok, J. D. *et al.* Final, 10-Year Outcomes with Nivolumab plus Ipilimumab in Advanced Melanoma. *N*
430 *Engl J Med* (2024). https://doi.org:10.1056/NEJMoa2407417
431 2 Morad, G., Helmink, B. A., Sharma, P. & Wargo, J. A. Hallmarks of response, resistance, and toxicity to
432 immune checkpoint blockade. *Cell* **184**, 5309-5337 (2021). https://doi.org:10.1016/j.cell.2021.09.020
433 3 Doki, Y. *et al.* Nivolumab Combination Therapy in Advanced Esophageal Squamous-Cell Carcinoma. *N Engl*
434 *J Med* **386**, 449-462 (2022). https://doi.org:10.1056/NEJMoa2111380
435 4 Wolchok, J. D. *et al.* Overall Survival with Combined Nivolumab and Ipilimumab in Advanced Melanoma. *N*
436 *Engl J Med* **377**, 1345-1356 (2017). https://doi.org:10.1056/NEJMoa1709684
437 5 Sznol, M. *et al.* Pooled Analysis Safety Profile of Nivolumab and Ipilimumab Combination Therapy in Patients
438 With Advanced Melanoma. *J Clin Oncol* **35**, 3815-3822 (2017). https://doi.org:10.1200/JCO.2016.72.1167
439 6 Motzer, R. J. *et al.* Nivolumab plus Ipilimumab versus Sunitinib in Advanced Renal-Cell Carcinoma. *N Engl J*
440 *Med* (2018). https://doi.org:10.1056/NEJMoa1712126
441 7 Sharma, P. *et al.* Nivolumab Plus Ipilimumab for Metastatic Castration-Resistant Prostate Cancer:
442 Preliminary Analysis of Patients in the CheckMate 650 Trial. *Cancer Cell* **38**, 489-499 e483 (2020).
443 https://doi.org:10.1016/j.ccell.2020.08.007
444 8 Hellmann, M. D. *et al.* Nivolumab plus Ipilimumab in Lung Cancer with a High Tumor Mutational Burden. *N*
445 *Engl J Med* **378**, 2093-2104 (2018). https://doi.org:10.1056/NEJMoa1801946
446 9 Overman, M. J. *et al.* Durable Clinical Benefit With Nivolumab Plus Ipilimumab in DNA Mismatch Repair-
447 Deficient/Microsatellite Instability-High Metastatic Colorectal Cancer. *J Clin Oncol*, JCO2017769901 (2018).
448 https://doi.org:10.1200/JCO.2017.76.9901
449 10 Gao, J. *et al.* Neoadjuvant PD-L1 plus CTLA-4 blockade in patients with cisplatin-ineligible operable high-risk
450 urothelial carcinoma. *Nat Med* **26**, 1845-1851 (2020). https://doi.org:10.1038/s41591-020-1086-y
451 11 Scherpereel, A. *et al.* Nivolumab or nivolumab plus ipilimumab in patients with relapsed malignant pleural
452 mesothelioma (IFCT-1501 MAPS2): a multicentre, open-label, randomised, non-comparative, phase 2 trial.
453 *Lancet Oncol* **20**, 239-253 (2019). https://doi.org:10.1016/S1470-2045(18)30765-4
454 12 Johncilla, M. *et al.* Ipilimumab-associated Hepatitis: Clinicopathologic Characterization in a Series of 11
455 Cases. *Am J Surg Pathol* **39**, 1075-1084 (2015). https://doi.org:10.1097/PAS.0000000000000453
456 13 Chen, P. L. *et al.* Analysis of Immune Signatures in Longitudinal Tumor Samples Yields Insight into
457 Biomarkers of Response and Mechanisms of Resistance to Immune Checkpoint Blockade. *Cancer Discov* **6**,
458 827-837 (2016). https://doi.org:10.1158/2159-8290.CD-15-1545
459 14 Daud, A. I. *et al.* Tumor immune profiling predicts response to anti-PD-1 therapy in human melanoma. *J Clin*
460 *Invest* **126**, 3447-3452 (2016). https://doi.org:10.1172/JCI87324
461 15 Rosenberg, S. A. *et al.* Durable complete responses in heavily pretreated patients with metastatic
462 melanoma using T-cell transfer immunotherapy. *Clin Cancer Res* **17**, 4550-4557 (2011).
463 https://doi.org:10.1158/1078-0432.CCR-11-0116
464 16 Rohaan, M. W. *et al.* Tumor-Infiltrating Lymphocyte Therapy or Ipilimumab in Advanced Melanoma. *N Engl*
465 *J Med* **387**, 2113-2125 (2022). https://doi.org:10.1056/NEJMoa2210233
466 17 Sarnaik, A. A. *et al.* Lifileucel, a Tumor-Infiltrating Lymphocyte Therapy, in Metastatic Melanoma. *J Clin*
467 *Oncol* **39**, 2656-2666 (2021). https://doi.org:10.1200/JCO.21.00612
468 18 Schulz, O., Hammerschmidt, S. I., Moschovakis, G. L. & Forster, R. Chemokines and Chemokine Receptors in
469 Lymphoid Tissue Dynamics. *Annu Rev Immunol* **34**, 203-242 (2016). https://doi.org:10.1146/annurev-
470 immunol-041015-055649
471 19 Bedognetti, D. *et al.* CXCR3/CCR5 pathways in metastatic melanoma patients treated with adoptive therapy
472 and interleukin-2. *Br J Cancer* **109**, 2412-2423 (2013). https://doi.org:10.1038/bjc.2013.557
473 20 Chheda, Z. S., Sharma, R. K., Jala, V. R., Luster, A. D. & Haribabu, B. Chemoattractant Receptors BLT1 and
474 CXCR3 Regulate Antitumor Immunity by Facilitating CD8+ T Cell Migration into Tumors. *J Immunol* **197**,
475 2016-2026 (2016). https://doi.org:10.4049/jimmunol.1502376
476 21 Hoch, T. *et al.* Multiplexed imaging mass cytometry of the chemokine milieus in melanoma characterizes
477 features of the response to immunotherapy. *Sci Immunol* **7**, eabk1692 (2022).
478 https://doi.org:10.1126/sciimmunol.abk1692

22 Bell, B., Flores-Lovon, K., Cueva-Chicana, L. A. & Macedo, R. Role of chemokine receptors in gastrointestinal mucosa. *Int Rev Cell Mol Biol* **388**, 20-52 (2024). https://doi.org:10.1016/bs.ircmb.2024.02.003

23 Valdivia-Silva, J. & Chinney-Herrera, A. Chemokine receptors and their ligands in breast cancer: The key roles in progression and metastasis. *Int Rev Cell Mol Biol* **388**, 124-161 (2024). https://doi.org:10.1016/bs.ircmb.2024.07.002

24 Tang, Y., Hu, Y., Niu, Y., Sun, L. & Guo, L. CCL5 as a Prognostic Marker for Survival and an Indicator for Immune Checkpoint Therapies in Small Cell Lung Cancer. *Front Med (Lausanne)* **9**, 834725 (2022). https://doi.org:10.3389/fmed.2022.834725

25 Seitz, S. *et al.* CXCL9 inhibits tumour growth and drives anti-PD-L1 therapy in ovarian cancer. *Br J Cancer* **126**, 1470-1480 (2022). https://doi.org:10.1038/s41416-022-01763-0

26 Han, Y. *et al.* CXCL10 and CCL5 as feasible biomarkers for immunotherapy of homologous recombination deficient ovarian cancer. *Am J Cancer Res* **13**, 1904-1922 (2023).

27 Reschke, R. *et al.* Immune cell and tumor cell-derived CXCL10 is indicative of immunotherapy response in metastatic melanoma. *J Immunother Cancer* **9** (2021). https://doi.org:10.1136/jitc-2021-003521

28 Fei, L., Ren, X., Yu, H. & Zhan, Y. Targeting the CCL2/CCR2 Axis in Cancer Immunotherapy: One Stone, Three Birds? *Front Immunol* **12**, 771210 (2021). https://doi.org:10.3389/fimmu.2021.771210

29 Velasco-Velazquez, M. *et al.* CCR5 antagonist blocks metastasis of basal breast cancer cells. *Cancer research* **72**, 3839-3850 (2012). https://doi.org:10.1158/0008-5472.CAN-11-3917

30 Sicoli, D. *et al.* CCR5 receptor antagonists block metastasis to bone of v-Src oncogene-transformed metastatic prostate cancer cell lines. *Cancer research* **74**, 7103-7114 (2014). https://doi.org:10.1158/0008-5472.CAN-14-0612

31 Halama, N. *et al.* Tumoral Immune Cell Exploitation in Colorectal Cancer Metastases Can Be Targeted Effectively by Anti-CCR5 Therapy in Cancer Patients. *Cancer Cell* **29**, 587-601 (2016). https://doi.org:10.1016/j.ccell.2016.03.005

32 Bachelerie, F. *et al.* International Union of Basic and Clinical Pharmacology. [corrected]. LXXXIX. Update on the extended family of chemokine receptors and introducing a new nomenclature for atypical chemokine receptors. *Pharmacol Rev* **66**, 1-79 (2014). https://doi.org:10.1124/pr.113.007724

33 Saltz, J., Gupta, R., Hou, L., Kurc, T., Singh, P., Nguyen, V., Samaras, D., Shroyer, K. R., Zhao, T., Batiste, R., Van Arnam, J., The Cancer Genome Atlas Research Network, Shmulevich, I., Rao, A. U. K., Lazar, A. J., Sharma, A., & Thorsson, V. Tumor-Infiltrating Lymphocytes Maps from TCGA H&E Whole Slide Pathology Images [Data set]. (2018). https://doi.org:10.7937/K9/TCIA.2018.Y75F9W1

34 Wolf, D. Immune Signature Scores [Data set, https://pancanatlas.xenahubs.net]. (2016).

35 Thorsson, V. *et al.* The Immune Landscape of Cancer. *Immunity* **51**, 411-412 (2019). https://doi.org:10.1016/j.immuni.2019.08.004

36 Gartrell, R. D. *et al.* Validation of Melanoma Immune Profile (MIP), a Prognostic Immune Gene Prediction Score for Stage II-III Melanoma. *Clin Cancer Res* **25**, 2494-2502 (2019). https://doi.org:10.1158/1078-0432.CCR-18-2847

37 Liu, D. *et al.* Integrative molecular and clinical modeling of clinical outcomes to PD1 blockade in patients with metastatic melanoma. *Nat Med* **25**, 1916-1927 (2019). https://doi.org:10.1038/s41591-019-0654-5

38 Tirosh, I. *et al.* Dissecting the multicellular ecosystem of metastatic melanoma by single-cell RNA-seq. *Science* **352**, 189-196 (2016). https://doi.org:10.1126/science.aad0501

39 Pozniak, J. *et al.* A TCF4-dependent gene regulatory network confers resistance to immunotherapy in melanoma. *Cell* **187**, 166-183 e125 (2024). https://doi.org:10.1016/j.cell.2023.11.037

40 Saelens, W., Cannoodt, R., Todorov, H. & Saeys, Y. A comparison of single-cell trajectory inference methods. *Nat Biotechnol* **37**, 547-554 (2019). https://doi.org:10.1038/s41587-019-0071-9

41 Yanagihara, T., Tanaka, K. & Matsumoto, K. A measuring method for occupancy of immune checkpoint inhibitors in the cell surface. *Biochem Biophys Res Commun* **527**, 213-217 (2020). https://doi.org:10.1016/j.bbrc.2020.04.122

42 Wong, M. T. *et al.* A High-Dimensional Atlas of Human T Cell Diversity Reveals Tissue-Specific Trafficking and Cytokine Signatures. *Immunity* **45**, 442-456 (2016). https://doi.org:10.1016/j.immuni.2016.07.007

43 Berahovich, R. D., Lai, N. L., Wei, Z., Lanier, L. L. & Schall, T. J. Evidence for NK cell subsets based on chemokine receptor expression. *J Immunol* **177**, 7833-7840 (2006). https://doi.org:10.4049/jimmunol.177.11.7833

532 44 Franciszkiewicz, K., Boissonnas, A., Boutet, M., Combadiere, C. & Mami-Chouaib, F. Role of chemokines and
533 chemokine receptors in shaping the effector phase of the antitumor immune response. *Cancer Res* **72**,
534 6325-6332 (2012). https://doi.org:10.1158/0008-5472.CAN-12-2027
535 45 Ozga, A. J., Chow, M. T. & Luster, A. D. Chemokines and the immune response to cancer. *Immunity* **54**, 859-
536 874 (2021). https://doi.org:10.1016/j.immuni.2021.01.012
537 46 Haghverdi, L., Buettner, F. & Theis, F. J. Diffusion maps for high-dimensional single-cell analysis of
538 differentiation data. *Bioinformatics* **31**, 2989-2998 (2015). https://doi.org:10.1093/bioinformatics/btv325
539 47 Villablanca, E. J. & Mora, J. R. Competitive homing assays to study gut-tropic t cell migration. *J Vis Exp* (2011).
540 https://doi.org:10.3791/2619
541 48 Anderson, K. G. *et al.* Intravascular staining for discrimination of vascular and tissue leukocytes. *Nat Protoc*
542 **9**, 209-222 (2014). https://doi.org:10.1038/nprot.2014.005
543 49 Aran, D. *et al.* Reference-based analysis of lung single-cell sequencing reveals a transitional profibrotic
544 macrophage. *Nat Immunol* **20**, 163-172 (2019). https://doi.org:10.1038/s41590-018-0276-y
545 50 Lopez, R., Regier, J., Cole, M. B., Jordan, M. I. & Yosef, N. Deep generative modeling for single-cell
546 transcriptomics. *Nat Methods* **15**, 1053-1058 (2018). https://doi.org:10.1038/s41592-018-0229-2
547

548 **Methods**

549 **Human samples**

550 All study participants signed a written informed consent before inclusion in the study, and the
551 protocols were approved by the Columbia University institutional review board (IRB). Peripheral
552 blood mononuclear cells (PBMCs) were obtained from melanoma patients by Ficoll gradients and
553 cryopreserved. PBMCs from healthy donors were obtained by Ficoll gradients and freshly
554 analyzed using spectral flow cytometry. Characteristics of patients and healthy donors are
555 summarized in Supplementary Table 4.

556 **Cell lines**

557 B16-F10 cell line was obtained from ATCC. B16-F10 cells were cultured at 37°C in Dulbecco's
558 Modified Eagle Media, supplemented with 10% FBS, 100 U ml^{-1} penicillin and 100 µg ml^{-1}
559 streptomycin, 2 mM L-glutamine. All cell lines were determined to be free of Mycoplasma (Lonza)
560 and common mouse pathogens (IDEXX).

561 ***In vivo* mouse studies**

562 All mice were used according to approved protocols by Columbia University Institutional Animal
563 Care and Use Committee (IACUC). Female mice, including C57BL/6J (B6) (Jax #000664), B6.129P2-
564 *Ccr5*^{tm1Kuz}/J (Jax #005427), B6.129P2-*Cxcr6*^{tm1Litt}/J (Jax #005693), B6.129P2-*Cxcr3*^{tm1Dgen}/J (Jax
565 #005796), and B6.SJL-*Ptprc*^{a}*Pepc*^{b}/BoyJ (Jax #002014) were obtained from The Jackson
566 Laboratory at 7-12 weeks of age and were used for studies one week or more after their arrival
567 in the animal barrier facility of the Columbia Center for Translational Immunology. For B16-F10
568 melanoma, 1×10^5 B16-F10 cells diluted in PBS were mixed with an equal volume of Matrigel
569 (Corning) and subcutaneously injected in the right flank of B6 mice on day 0. Blocking antibodies
570 were given on days 5, 8 and 11 after tumor implantation. Antibodies used for *in vivo* immune
571 checkpoint blockade experiments were given intraperitoneally at a dose of 200 mg per mouse
572 and included: CTLA4 (9H10) and PD-1 (RMP1-14) (BioXCell). Tumor diameters were measured
573 using calipers. Volume was calculated using the formula: (length × width^2)/2. Mice were
574 euthanized when tumor burden reached a volume of 1500 mm^3. Normalized tumor response to
575 treatment is the measured volume at time t (Vt) relative to volume at baseline (Vo).

576 **Preparation of murine single-cell suspensions for flow cytometry**

577 Murine cell suspensions were obtained from tumors or livers by a combination of GentleMACS
578 (Miltenyi Biotec) dissociation and enzymatic dissociation using 1 mg/mL of collagenase IV (Sigma-
579 Aldrich) and 0.2 mg/mL of DNase (Roche), followed by incubation with ACK Lysis buffer (Life
580 Technologies) for 1 minute to remove red blood cells. For tumor-draining lymph nodes,
581 mechanical and enzymatic dissociation was performed. After enzymatic incubation, samples
582 were filtered through a 70-µm nylon cell strainer (Falcon). Splenocytes were obtained by
583 dissociation using a 70-µm nylon cell strainer (Falcon) followed by ACK lysis buffer incubation for
584 1 minute. Cell suspensions were counted using Trypan Blue for cell viability.

585 **Flow cytometry and cell sorting**

586 For flow cytometric analysis, live/dead cell discrimination was performed using Zombie NIR
587 Fixable Viability dye (Biolegend) or eFluor780 Fixable Viability Dye (eBiosciences). Fc receptors
588 were blocked using 2.4G2 anti-mouse CD16/CD32 (BD Pharmingen) or Human TruStain FcX
589 (Biolegend). Cell surface staining was done for 15 min at 36°C, followed by 15 min at 4°C.
590 Intracellular staining was done using a fixation/permeabilization kit (eBioscience). For human
591 cells, we used multiparametric spectral flow cytometry with a 43-color extracellular panel and
592 42-color intracellular panel that allowed us to study multiple leukocyte populations, CRs, and
593 functional markers simultaneously. In a similar way, for murine cells we used a 36-color
594 extracellular panel and a 35-color intracellular panel to study multiple leukocyte populations,
595 CRs, and other markers. For certain murine experiments traditional flow cytometry was used to
596 identify T cell populations. All flow cytometric analyses were performed using Aurora 5 lasers
597 (Cytek) or Fortessa II (BD) and analyzed using FlowJo software (BD). Cell sorting of CR-defined
598 subsets was performed using an Influx Cell Sorter (BD). Human and murine sorted cells were
599 stained with CellTrace kit followed by stimulation with Phorbol 12-myristate 13-acetate (PMA)
600 for 2 hours to study activation or 2 days for proliferation. See Supplementary Table 3 for a list of
601 antibodies used.

602 **Competitive homing experiment**

603 To determine the role of each individual CR in homing and tissue-infiltration of T cells, we
604 performed a competitive short-term homing strategy [47] to identify four groups of cells injected
605 at identical proportions. First, we treated WT, CCR5$^{-/-}$, CXCR6$^{-/-}$, or CXCR3 -/- mice with anti-PD-1
606 + anti-CTLA-4 (P1C4) or PBS on days 5, 8, and 11. On Day 12, mice were euthanized, and T cells
607 were isolated from the spleen using Pan T Cell Isolation Kit II (Miltenyi Biotec). After labelling T
608 cells with different CellTrace Kits (except R6$^{-/-}$ mice which express GFP reporter) and combining
609 them at similar proportion, 15×10^6 T cells were injected into the tail vein of B16 tumor-bearing
610 PepBoy mice (Day 12 after tumor injection), also treated with PBS or P1C4 following the same
611 treatment schedule and respecting the same group (PBS in PBS, P1C4 in P1C4). After 48 hours
612 recipient mice were intravenously injected with anti-CD90.2 antibody for discrimination between
613 vascular (circulating) and tissue lymphocytes [48]. After 3 minutes, mice were sacrificed, and the
614 percentage of WT, CCR5$^{-/-}$, CXCR6$^{-/-}$, or CXCR3$^{-/-}$ in CD45.2$^+$ CD3$^+$ cells in each tissue was divided
615 by the percentage of the same cells before injection.

616 **Immunohistochemistry of mouse tissues**

617 For liver immunohistochemistry, rabbit anti-CD3ε antibody (Invitrogen SP7) was diluted 1:100
618 and incubated at room temperature for 2 hours. Signal amplification was performed using
619 ImmPRESS Horse anti-rabbit IgG antibody-HRP (Vector) and DAB substrate Kit (BD Pharmingen)
620 following the manufacturer's protocol. Slides were counterstained and mounted.

621 **TCGA RNAseq**

622 RNAseq data was downloaded from the TCGA Pan-Cancer and TCGA Melanoma (SKCM) cohorts
623 from xenabrowser.net [51] (IDs: EB++AdjustPANCAN_IlluminaHiSeq_RNASeqV2.geneExp.xena and
624 TCGA.SKCM.sampleMap/HiSeqV2; unit: log2(norm_count + 1)), and corresponding phenotype
625 datasets (IDs: Survival_SupplementalTable_S1_20171025_xena_sp, survival/SKCM_survival.txt,

626 TCGA_phenotype_denseDataOnlyDownload.tsv, TCGA.SKCM.sampleMap/SKCM_clinicalMatrix).
627 This dataset contained 11060 samples for PANCAN and 464 samples for SKCM, but only primary
628 and metastatic tumors were analyzed (n=10272 for PANCAN, n=104 for primary SKCM, and n=368
629 for metastatic SKCM). R value from Pearson correlation between normalized RSEM counts (> 5
630 log2(x+1)) of CRs/ligands and cell-type-specific genes (Supplementary Table 1; based on Tirosh
631 et al) was calculated using GraphPad Prism v10. Then, an unsupervised hierarchical clustering
632 gene tree was generated based on these correlations using Multi Experiment Viewer (MeV) v4.9
633 [52]. For combinatorial CR scores, *CXCR6*, *CXCR3* and *CCR5* normalized gene expression were
634 averaged (Score 1), or *CCR5* normalized gene expression was subtracted from *CXCR6* and *CXCR3*
635 normalized gene expression sum (Score 2). For survival analysis, optimal cutoffs were calculated
636 using Kaplan-Meier Plotter (kmplot.com) [53], and Kaplan-Meier curves and Log-rank p values were
637 generated using GraphPad Prism v10. Identification of upregulated differentially expressed genes
638 from TCGA and Liu *et al* primary melanoma samples was done using SeqGeq (BD), a platform that
639 allows visualization of scRNA seq data and RNA seq data. STRING database (https://string-
640 db.org/), was used to generate biological process gene ontology analysis [54].

641 **Analysis of publicly available single-cell datasets**

642 To perform an *in-silico* analysis of single-cell RNA seq data from human metastatic melanoma,
643 the GSE72056_melanoma_single_cell_revised_v2.txt.gz file was downloaded from GEO Series
644 GSE72056. Using SeqGeq (BD), a characterization of immune and non-immune cells in the TME
645 was performed with UMAP multidimensional analysis. Subsets were defined in $CD8^+$ T cells by
646 the co-expression of *CCR7*, *CXCR6*, *CXCR3* and *CCR5* following the gating strategy defined in Fig.
647 1d left. Finally, gene expression of other functional markers was measured within CR-defined
648 subsets.

649 **scRNA-seq analysis of external clinical melanoma cohort immune cells**

650 Pre-processed scRNA-seq datasets of immune cells (n=49,009) from patients studied in Pozniak
651 et. al [39] were loaded into Seurat in R and subsequently Scanpy in Python. Immune cell annotation
652 was guided by automatic annotation using SingleR and its built-in reference dataset of stroma
653 and immune cells 'BlueprintEncodeData' as previously described [49]. Non-cycling $CD8^+$ T cell
654 subtypes (n=13,304) were selected for downstream analysis in Scanpy. The top 8,000 highly
655 variable genes were calculated using the 'Seurat_V3' method implemented in Scanpy. Gene
656 expression counts were normalized to median total counts and logarithmized in Scanpy. $CD8^+$ T
657 cells from individual samples were batch corrected using an scVI model trained with two hidden
658 layers and 30-dimensional latent space [50]. After performing neighborhood graph construction
659 using 20 nearest neighbors in scVI latent space, leiden clustering with default resolution, and
660 evaluation of known marker genes and $CD8^+$ T cell gene signatures in Scanpy, a noisy outlier
661 cluster was removed to prevent distortions in subsequent diffusion maps. Then, after
662 reconstructing the neighborhood graph using 300 nearest neighbors in scVI space, we computed
663 diffusion components (DCs) using the Scanpy implementation to examine continuous phenotypic
664 dynamics. The first and second DCs reflected expected *TCF7*$^+$ to *TOX*$^+$ progression of $CD8^+$ T cells,
665 and diffusion pseudotime along this trajectory was computed using the Scanpy implementation
666 to reflect this progression. We then plotted the expression of *CCR7*, *CXCR3*, *CCR5*, and *CXCR6*
667 across pseudotime using $CD8^+$ T cells ordered by diffusion pseudotime rank. Given the sparsity of

668 CR expression, which is typical for a clinical scRNA-seq dataset, we used sliding windows of 300
669 cells to average normalized expression across the $CD8^+$ T cell trajectory. We also computed the
670 95% confidence interval on the same window of 300 cells to reflect variation in expression across
671 the trajectory. The window size of 300 reduced sparsity while still conserving the expected
672 negative binomial distribution of CR gene expression counts. To compare CR expression patterns
673 over $CD8^+$ T cell trajectory, expression of each CR was scaled and plotted across cell pseudotime
674 rank, reflecting the expected progression of *CCR7*$^+$ to *CXCR6*$^+$ expression in $CD8^+$ T cells. Finally,
675 we examined differential expression of CR genes and the R6 co-expressing signatures (R6R3,
676 R6R5, R6R3R5) across ICB responder/non-responder clinical groups using average gene
677 expression pseudobulked by sample (summation of counts in each sample divided by total
678 number of cells in each sample) to account for CR expression sparsity and intrapatient
679 heterogeneity. Pseudobulked sample gene expression and signature expression were compared
680 across clinical groups using boxplots and significance was assessed using Mann-Whitney U-tests.
681 Code relating to this data analysis is publicly available on GitHub:
682 https://github.com/azizilab/chemokine_receptor_reproducibility.

683 **Statistical analysis**

684 One-way ANOVA was used for normally distributed data. Mann–Whitney was used for non-
685 parametric data. Kaplan–Meier log-rank analysis was used to evaluate the survival differences
686 between groups. Statistical analysis was conducted using Prism 10.0 software (GraphPad). Only
687 p values < 0.05 were considered as significant.

688 **Methods Bibliography.**

689 51. Goldman, M.J., Craft, B., Hastie, M. et al. Visualizing and interpreting cancer genomics data
690 via the Xena platform. Nat Biotechnol (2020). https://doi.org/10.1038/s41587-020-0546-8

691 52. Saeed AI, Sharov V, White J, Li J, Liang W, Bhagabati N, Braisted J, Klapa M, Currier T,
692 Thiagarajan M, Sturn A, Snuffin M, Rezantsev A, Popov D, Ryltsov A, Kostukovich E, Borisovsky I,
693 Liu Z, Vinsavich A, Trush V, Quackenbush J. TM4: a free, open-source system for microarray data
694 management and analysis. Biotechniques. 2003 Feb;34(2):374-8

695 53. Lanczky A, Gyorffy B. Web-Based Survival Analysis Tool Tailored for Medical Research
696 (KMplot): Development and Implementation, J Med Internet Res, 2021; 23(7):e27633,
697 doi:10.2196/27633

698 54. Szklarczyk D, Kirsch R, Koutrouli M, Nastou K, Mehryary F, Hachilif R, Gable AL, Fang T,
699 Doncheva NT, Pyysalo S, Bork P, Jensen LJ, von Mering C. The STRING database in 2023: protein-
700 protein association networks and functional enrichment analyses for any sequenced genome of
701 interest. Nucleic Acids Res. 2023 Jan 6;51(D1):D638-D646. doi: 10.1093/nar/gkac1000.